In the active state, it assumes a random coil conformation with a short helical segment (residues 202 to 206) (Fig. 2A) loosely connecting regulatory and catalytic domains. High B factors in this region are consistent with a high mobility that allows the catalytic domains to assemble both active sites. In the inhibited state, this segment forms an α helix with low B values, extending the αN10-helix of the regulatory domain by 24 Å or four turns (Fig. 2B) to keep the catalytic domains apart. The newly formed helical turns participate in the interface between regulatory and catalytic domains. To test whether the integrity of the helical segment is a prerequisite of pH regulation, two consecutive prolines were introduced at the beginning of the αN10-switch. Because of their restricted Φ and Ψ-values, this was not compatible with an α-helical conformation (*20*). In the M193P/M194P double mutant, pH regulation was lost, and the activity of the mutant holoenzyme over the pH range of 5.5 to 8 is similar to that of activated wild-type protein at pH 5.5 (Fig. 1B). Thus, the extension of the αN10 switch helix is a determinant of the inhibited state.

Two residues in the αN10-switch helix, identified by mutagenesis, are important for the interaction between the regulatory and catalytic domains (Fig. 4C). One site of interaction comprises Asp^{62}, Tyr^{66}, Glu^{195}, and Arg^{309} (Fig. 4A). The arginine points into a crevice in the regulatory domain and organizes the other residues through formation of hydrogen bonds. An R309A mutation renders the holoenzyme active and unregulated (Fig. 1C). The same mutation in the isolated catalytic domain ($Rv1264_{211\text{-}397}$R309A) has no effect (*21*). Additionally, an E195A mutation partially relieves the inhibition, results in a fourfold increase in activity at pH 8.0, and shifts the pH optimum from pH 5.8 to pH 6.5 (Fig. 1C). A further site of interaction at the beginning of the αN10-switch helix forms around His^{192} (Fig. 4B). The catalytic residues Lys^{261} and Asp^{312} are held 14 Å and 21 Å away from their respective positions in the active state by an interaction with His^{192} (Figs. 3C and 4B). A H192A mutant shows the wild-type phenotype at pH 8, but the slope of activation is shifted by 0.5 pH units toward the acidic pH (Fig. 1D). At acidic pH, His^{192} is expected to be protonated, and the positive charge may result in electrostatic repulsion of Lys^{261}. Similarly, a H192E mutant has a 10-fold higher activity at pH 8.0 than the wild-type protein, indicating that a negative charge at this position interferes with Asp^{312} (Fig. 1D). The data indicate that there is no designated, single amino acid residue that acts as a pH receptor, but that a network of hydrogen and ionic bonds in the interface between catalytic and regulatory domains mediate pH sensitivity and responsiveness.

Because of the structural similarities between the catalytic domains of both AC Rv1264 and mammalian ACs, the α1 and the αN10 switch regions may be prototypical regulatory elements for class III ACs. In the active state of Rv1264, the catalytic domains align even in the absence of bound nucleotide, whereas the regulatory domains effectively impede this alignment in the inhibited state. The comparison with mammalian enzymes shows that, in all class III ACs, activity is tuned by the alignment of the catalytic dimer. The mode of interaction may differ, but the repositioning of catalytic domains organized by a common structural switch may prove to be a general principle as more AC holoenzyme structures become available.

References and Notes

1. O. Barzu, A. Danchin, *Prog. Nucleic Acid Res. Mol. Biol.* **49**, 241 (1994).
2. J. U. Linder, J. E. Schultz, *Cell. Signal.* **15**, 1081 (2003).
3. D. A. Baker, J. M. Kelly, *Mol. Microbiol.* **52**, 1229 (2004).
4. S. T. Cole *et al.*, *Nature* **393**, 537 (1998).
5. L. A. McCue, K. A. McDonough, C. E. Lawrence, *Genome Res.* **10**, 204 (2000).
6. W. F. Simonds, *Trends Pharmacol. Sci.* **20**, 66 (1999).
7. D. M. F. Cooper, *Biochem. J.* **375**, 517 (2003).
8. J. U. Linder, A. Schultz, J. E. Schultz, *J. Biol. Chem.* **277**, 15271 (2002).
9. U. Süsstrunk, J. Pidoux, S. Taubert, A. Ullmann, C. J. Thompson, *Mol. Microbiol.* **30**, 33 (1998).
10. S. Sturgill-Koszycki *et al.*, *Science* **263**, 678 (1994).
11. K. Pethe *et al.*, *Proc. Natl. Acad. Sci. U.S.A.* **101**, 13642 (2004).
12. Materials and methods are available as supporting material on *Science* Online.
13. The inhibited form of Rv1264 was determined from a crystal grown at pH 5.5 and the active form from a crystal grown at pH 7.5. These pH values are in contrast to the activity assays. A discrepancy between crystallization conditions and activity assays is not unusual, however; the structure of the $G_s\alpha$-activated mammalian AC (1CJK) (*16*) has been crystallized at pH 5.4, two units below the pH of both the in vivo environment of the enzyme and the in vitro activity assay. Rv1264 exists in equilibrium between active and inhibited states that are governed by pH in our in vitro assay (Fig. 1A). For crystallization, other factors such as the different dielectric constants (PEG400 versus Li_2SO_4) can override the effect of pH on this equilibrium. Indeed, both the active and inhibited states of Rv1264 crystallize at the same pH: The needle-shaped crystals of the active state are obtained over a pH range from pH 5.4 to pH 7.5. These crystals all have the same distinctive morphology, which strongly suggests that they all represent the enzyme in the active state, and are easily distinguished from those crystals of the enzyme in the inhibited state. The needle-shaped crystals are usually 1 to 5 μm in diameter and not suitable for diffraction analysis, but one crystal grown to a diameter of ~20 μm at pH 7.5 diffracted to 3.3 Å at the beamline ID13 in Grenoble.
14. F. Findeisen *et al.*, unpublished data.
15. G. Zhang, Y. Liu, A. E. Ruoho, J. H. Hurley, *Nature* **386**, 247 (1997).
16. J. J. Tesmer, R. K. Sunahara, A. G. Gilman, S. R. Sprang, *Science* **278**, 1907 (1997).
17. W.-J. Tang, J. H. Hurley, *Mol. Pharmacol.* **54**, 231 (1998).
18. J. J. Tesmer *et al.*, *Biochemistry* **39**, 14464 (2000).
19. J. J. Tesmer *et al.*, *Science* **285**, 756 (1999).
20. K. T. O'Neil, W. F. DeGrado, *Science* **250**, 646 (1990).
21. I. Tews *et al.*, unpublished data.
22. W. L. DeLano (DeLano Scientific, San Carlos, CA, 2002), available at www.pymol.org.

23. Data collection was performed at beamlines ID13 and ID14-4 (European Synchrotron Radiation Facility, Grenoble). Supported by the Deutsche Forschungsgemeinschaft (grant nos. TE368/1-1 and LI928/2-1). Structure coordinates have been deposited in the Protein Data Bank under accession codes 1Y10 (inhibited state) and 1Y11 (active state).

Supporting Online Material

www.sciencemag.org/cgi/content/full/308/5724/1020/DC1
Materials and Methods
Figs. S1 and S2
Table S1
References and Notes
Movie S1

17 November 2004; accepted 1 March 2005
10.1126/science.1107642

Structural Basis of Energy Transduction in the Transport Cycle of MsbA

Jinhui Dong, Guangyong Yang, Hassane S. Mchaourab*

We used site-directed spin-labeling and electron paramagnetic resonance spectroscopy to characterize the conformational motion that couples energy expenditure to substrate translocation in the multidrug transporter MsbA. In liposomes, ligand-free MsbA samples conformations that depart from the crystal structures, including looser packing and water penetration along the periplasmic side. Adenosine triphosphate (ATP) binding closes the substrate chamber to the cytoplasm while increasing hydration at the periplasmic side, consistent with an alternating access model. Accentuated by ATP hydrolysis, the changes in the chamber dielectric environment and its geometry provide the likely driving force for flipping amphipathic substrates and a potential exit pathway. These results establish the structural dynamic basis of the power stroke in multidrug-resistant ATP-binding cassette (MDR ABC) transporters.

ABC transporters transduce the energy of ATP binding and hydrolysis into the mechanical work of substrate translocation across cell membranes (*1*–*3*). The functional unit consists of two nucleotide binding and hydrolysis domains (NBDs), each coupled to a

transmembrane domain (TMD) that encodes the determinants of substrate specificity and provides a pathway through the membrane. A subclass of ABC transporters, including P-glycoprotein (P-gp) and LmrA, consists of lipid efflux pumps that have been implicated in multidrug resistance (*4*–*7*). MsbA, an ABC *E. coli* transporter, transports lipid A across the inner membrane (*8*, *9*), and its adenosine triphosphate hydrolysis activity (ATPase) is stimulated by cytotoxic molecules (*10*). A prevalent mechanistic model of MDR ABC transporters links alternating ATP hydrolysis by each NBD domain to substrate transport through changes in orientation and affinity of the substrate-binding site(s) (*11*).

Two crystal structures of ligand-free MsbA define the molecular architecture of MDR ABC transporters (*12*, *13*). Obtained in detergent micelles, one structure consists of two monomers organized in an open conformation where the two TMDs pack asymmetrically to form a large V-shaped chamber open to the cytoplasm and the inner bilayer leaflet (Fig. 1A). In each monomer, the NBD and TMD are bridged by an intracellular domain (ICD). In the second structure, referred to as the closed conformation (Fig. 1C), rigid-body motion of the TMD and NBD occludes the chamber to the cytoplasm.

Although the two structures portray a flexible molecule and provide snapshots of the large conformational motion possible, the absence of ligands in the crystals does not allow interpretation of the structural differences in the context of the transport cycle. Furthermore, these static structures are not easily reconcilable with a body of biochemical and cross-linking studies of homologous proteins (*14*–*18*). The crystallization in two conformations and the discrepancies with solution constraints suggest that apo-MsbA is in a conformeric equilibrium.

We have investigated the structure of apo-MsbA in liposomes and mapped conformational changes during the ATPase cycle by electron paramagnetic resonance (EPR) analysis of 112 spin-labeled mutants (*19*) (Fig. 1A) trapped in four intermediate states. Spin-label mobilities, collisions with the paramagnetic reagents nickel(II) ethylenediaminediacetate (NiEDDA) and molecular oxygen, and spin-spin interactions were interpreted as constraints on the local steric environment, the accessibility to the bilayer and aqueous phases, and proximities between identical sites in the MsbA dimer, respectively (*20*).

The accessibility (*21*) data set of apo-MsbA, shown in Fig. 1B, defines the location and orientation of transmembrane helices and maps regions of aqueous solvation in the chamber and the periplasmic loops (labeled EC1 and EC3). We observed distinct patterns of oxygen accessibility [$\Pi(O_2)$], consisting of 3.6 residue periodicity with an amplitude gradient, that reflects the transmembrane orientation of helices 2 and 5 and their direct contact with the bilayer. In contrast, the lack of such a pattern along helix 6 suggests that this helix does not have a lipid-interacting surface. Supporting this conclusion is the restricted motion of the spin label at sites predicted to be exposed to the bilayer by the crystal structures (Fig. 2A). At the periplasmic side of the transporter, evidence of a loose structure includes an increase in $\Pi(O_2)$ and mobile line shapes (residues 271 and 274 in Fig. 2B) at the helix 5 C-terminal end and the adjacent EC3 loop, where monomer-monomer contacts occur in the crystal structures. Little if any broadening due to spin-spin interactions was detected at these sites.

The gradient of decreasing NiEDDA accessibility [Π(NiEDDA)], starting at chamber-facing residues in the ICD and the cytoplasmic ends of the helices, is in agreement with the spatial disposition of the monomers and the progressive narrowing of the chamber in the open

Department of Molecular Physiology and Biophysics, Vanderbilt University, Nashville, TN 37232, USA.

*To whom correspondence should be addressed. E-mail: hassane.mchaourab@vanderbilt.edu

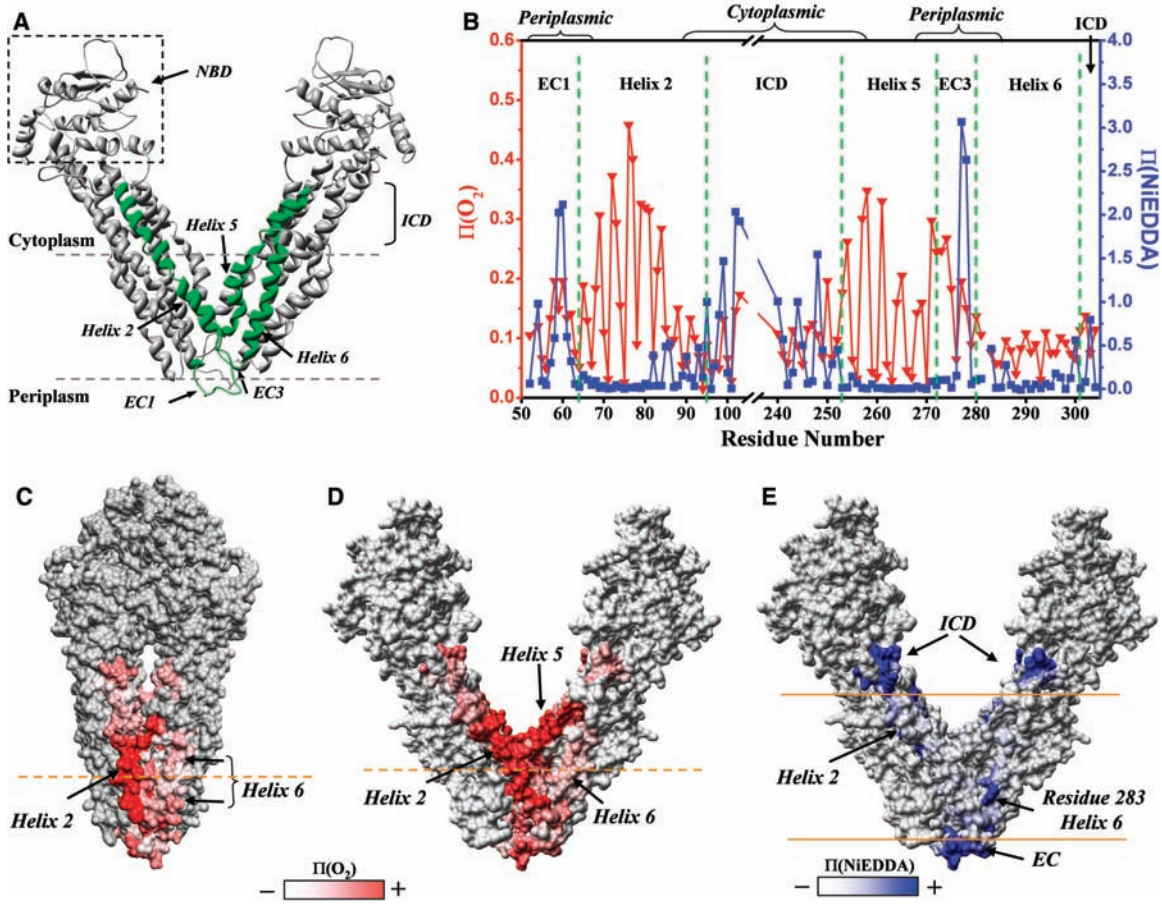

Fig. 1. (**A**) Ribbon representation of the structure of MsbA in the open state. Highlighted in green are the segments in a monomer subjected to cysteine substitution and spin labeling. (**B**) Accessibility profiles of apo-MsbA. Red, $\Pi(O_2)$; blue, Π(NiEDDA). The dotted green lines indicate the boundaries of the helices and loops on the basis of the crystal structure assignment. (**C** and **D**) $\Pi(O_2)$ mapped onto a surface rendering of the closed and open states, respectively. The dashed line through residue 76 defines the middle of the bilayer. (**E**) Π(NiEDDA) mapped onto a surface rendering of the open state. The solid orange lines represent the boundaries of the bilayer deduced from the onset of in-phase oscillations of $\Pi(O_2)$ and Π(NiEDDA) along helix 2. Surface representations were produced with Chimera (*34*).

structure (Fig. 1, A and B). Significant NiEDDA accessibility continues into the transmembrane domain including residues such as 82, one turn away from the middle of the bilayer defined by the absolute maximum in $\Pi(O_2)$ at residue 76.

The trend of looser packing at the periplasmic side of the transporter corresponds with significant NiEDDA accessibility along the N-terminal end of helix 6 (e.g., residues 283, 286), EC3, and to a lesser extent the 271 to 274 stretch, all of which are predicted by the crystal structures to be within the confines of the bilayer. Patterns of Π(NiEDDA) and proximities in EC1 also suggest deviations from the open and closed states. For instance, strong spin-spin interactions at residue 57 (Fig. 2C) and, to a lesser extent, at residues 52 and 58 (*22*) do not reflect the pattern of relative proximities observed in the crystal structures. Multiple conformations of this loop are implied by the composite nature of the EPR spectrum at site 57.

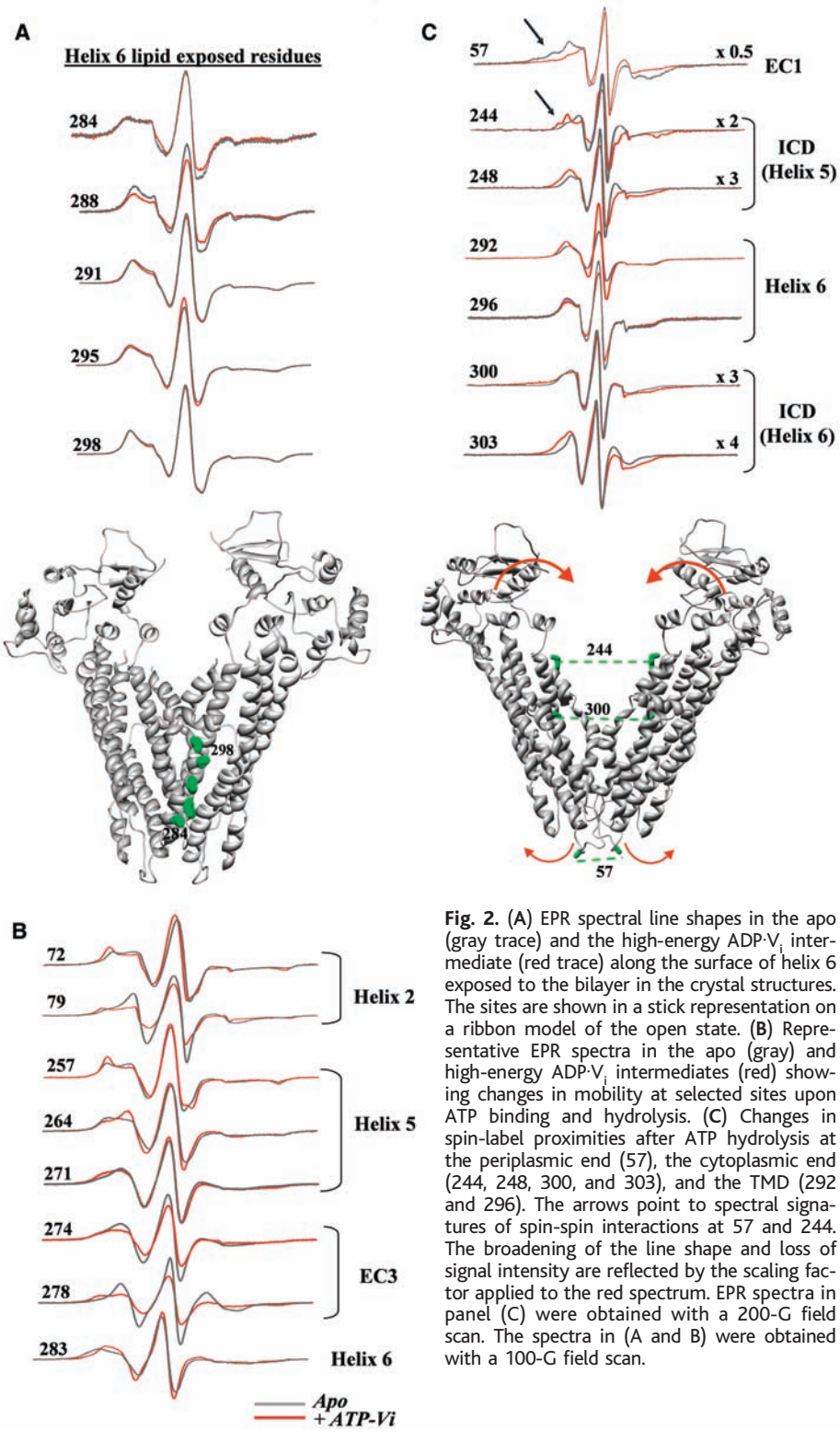

Fig. 2. (**A**) EPR spectral line shapes in the apo (gray trace) and the high-energy ADP·V_i intermediate (red trace) along the surface of helix 6 exposed to the bilayer in the crystal structures. The sites are shown in a stick representation on a ribbon model of the open state. (**B**) Representative EPR spectra in the apo (gray) and high-energy ADP·V_i intermediates (red) showing changes in mobility at selected sites upon ATP binding and hydrolysis. (**C**) Changes in spin-label proximities after ATP hydrolysis at the periplasmic end (57), the cytoplasmic end (244, 248, 300, and 303), and the TMD (292 and 296). The arrows point to spectral signatures of spin-spin interactions at 57 and 244. The broadening of the line shape and loss of signal intensity are reflected by the scaling factor applied to the red spectrum. EPR spectra in panel (C) were obtained with a 200-G field scan. The spectra in (A and B) were obtained with a 100-G field scan.

To evaluate the compatibility of the EPR constraints with the crystal structures, the accessibility parameters were mapped onto the open and closed conformations (Fig. 1, C, D, and E). Extensive NiEDDA accessibility and lack of spin-spin interactions support a dominant openlike conformation or ensemble of conformations at the cytoplasmic end, whereas along the periplasmic side, where crystal contacts occur, the data set indicates a more open structure and the presence of hydrated regions in the membrane. Aqueous solvation in the transmembrane part of the chamber was also deduced from accessibility studies of LmrA (*23*) and P-gp (*24*). Our data disagree with the conclusion of Buchaklian *et al*. (*25*) that the MsbA chamber is not accessible to water. The source of this discrepancy may be their limited sampling of the chamber, as they examined the accessibility of only two sites.

In the TMD, $\Pi(O_2)$ and the mobility pattern (fig. S1A) of helix 2 are in general agreement with its peripheral location and orientation relative to the bilayer, although its NiEDDA-exposed surface appears to be rotated away from the chamber and in contact with a neighboring helix (Fig. 1E). A similar phase-shift along helix 5 results in the maxima of $\Pi(O_2)$ (residues 257 and 258) partly facing the chamber. The most intriguing discrepancy occurs in a region of helix 6 (residues 283 to 290), where the EPR constraints are incompatible with the extensive bilayer contact of this helix in both crystal structures. The simplest model implied by the EPR constraints has helix 6 displaced toward the interior of the dimer, where it is in tertiary contacts with neighboring helices. This model is supported by spin-spin interactions at sites 292 and 296 (Fig. 2C), which are not predicted by the open conformation and the uniformly restricted mobilities of the spin label along the helix (*22*).

An alternative model that resolves these inconsistencies is based on a recent crystal structure of MsbA that shows the binding of a lipid A molecule at the surface of helix 6 (*26*). Specific contacts with a substrate molecule may explain the immobilized line shapes and the lower oxygen accessibility but not the spin-spin interaction pattern. The substrate in our samples could be a lipid A molecule copurified with the transporter, or the binding site may be occupied by phosphatidylethanolamine, a component of our reconstitution mixture that was shown to be transported by MsbA (*27*).

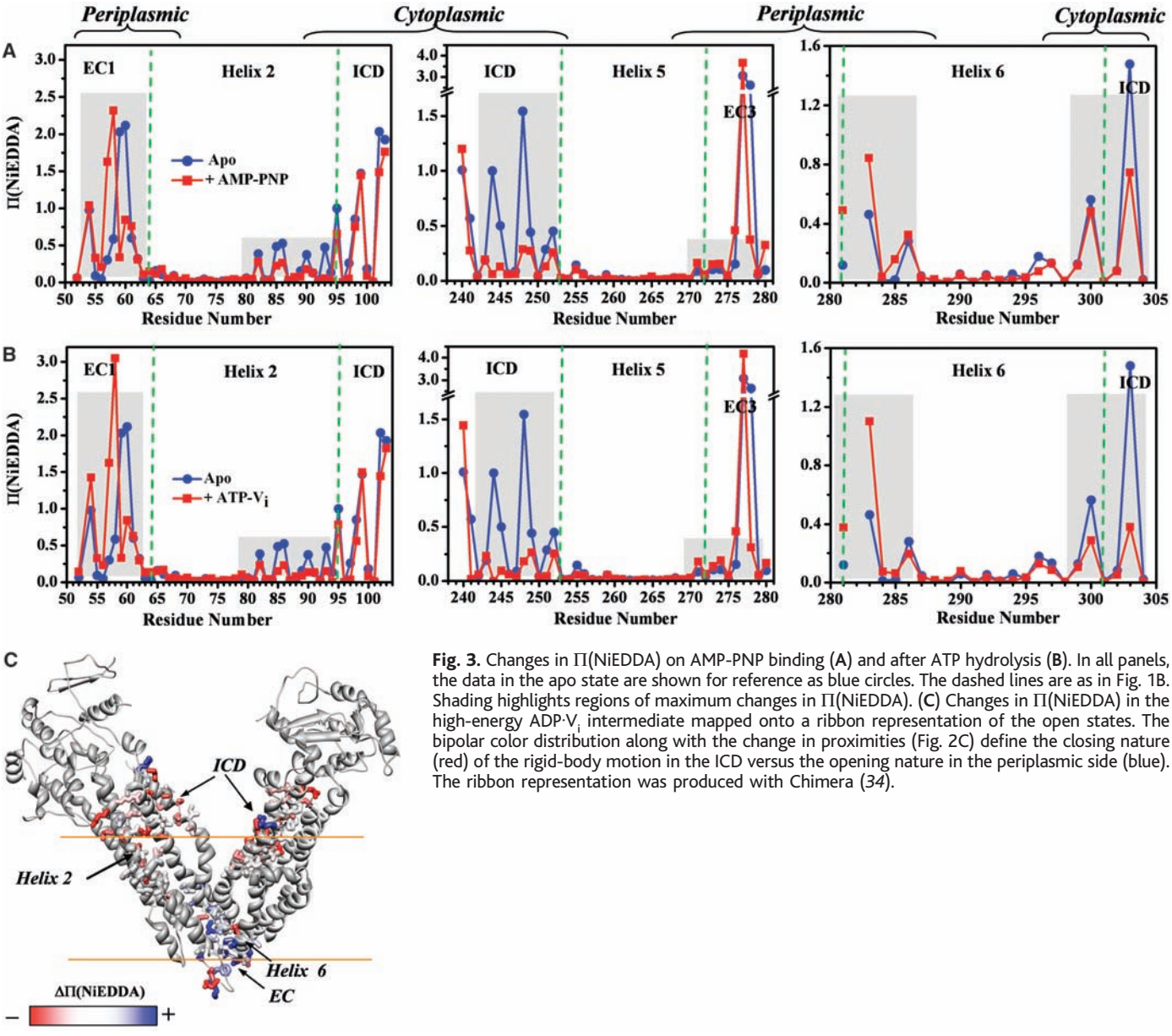

Fig. 3. Changes in Π(NiEDDA) on AMP-PNP binding (**A**) and after ATP hydrolysis (**B**). In all panels, the data in the apo state are shown for reference as blue circles. The dashed lines are as in Fig. 1B. Shading highlights regions of maximum changes in Π(NiEDDA). (**C**) Changes in Π(NiEDDA) in the high-energy ADP·V_i intermediate mapped onto a ribbon representation of the open states. The bipolar color distribution along with the change in proximities (Fig. 2C) define the closing nature (red) of the rigid-body motion in the ICD versus the opening nature in the periplasmic side (blue). The ribbon representation was produced with Chimera (*34*).

Overall, our analysis reinforces the model that apo-MsbA is in an equilibrium that includes conformers besides the two crystallized so far. Indeed, the extent of opening at the periplasmic side in these conformers may be understated by the averaging of the NiEDDA accessibilities over a heterogeneous ensemble. Although the EPR data set is not indicative of a highly populated closed state in the ensemble, the averaging may also understate this population in our analysis. The dynamic partitioning of MsbA among these conformers may account for the phase differences in the accessibility of helices.

The trajectory of the average structure and the corresponding shifts in the conformeric equilibrium during the functional cycle have been captured by the changes in the EPR parameters in three nucleotide-bound intermediates (*11*, *28*, *29*). The ATP-bound state is trapped by binding of the nonhydrolyzable analog AMP-PNP. Two post hydrolysis states, i.e., adenosine diphosphate (ADP)–bound states, were stabilized by inorganic vanadate (V_i) addition after either ATP or ADP binding. V_i acts as a γ-phosphate analog and, along with ADP, forms a complex mimicking the transition state of ATP hydrolysis. Studies of the ABC transporters P-gp and MalK demonstrate that a high-energy ADP-bound intermediate is more readily trapped by V_i after ATP hydrolysis than by direct ADP addition (*28*, *29*).

Changes in Π(NiEDDA) upon nucleotide binding are shown in Fig. 3 and fig. S2. Parallel reduction along the ICD and cytoplasmic ends of helices 2, 5, and 6 reveals a global, conformational change upon AMP-PNP binding that occludes the substrate chamber. Occlusion is maintained and accentuated in the post hydrolysis state populated by adding V_i and ATP. Concomitant nucleotide-induced increase in spin-spin interactions at multiple sites in the ICD regions (Fig. 2C) indicates that reduced chamber accessibility is due to rigid-body motion that moves the spin labels into close proximity (less than 15 Å). The pattern of proximity change is in overall agreement with the direction of the domain movement observed in the closed state, although the relative strengths of spin-spin interactions are not.

The opposite pattern of accessibility and proximity changes are observed at the periplasmic side of the transporter. The two EC1 loops undergo conformational changes that increase the distance between residues 57 (Fig. 2C) and 58 from different subunits and alter the NiEDDA accessibility in the 57 to 61 stretch (Fig. 3A). The loop movement allows increased NiEDDA accessibility at the periplasmic sides of helix 5 (C terminus),

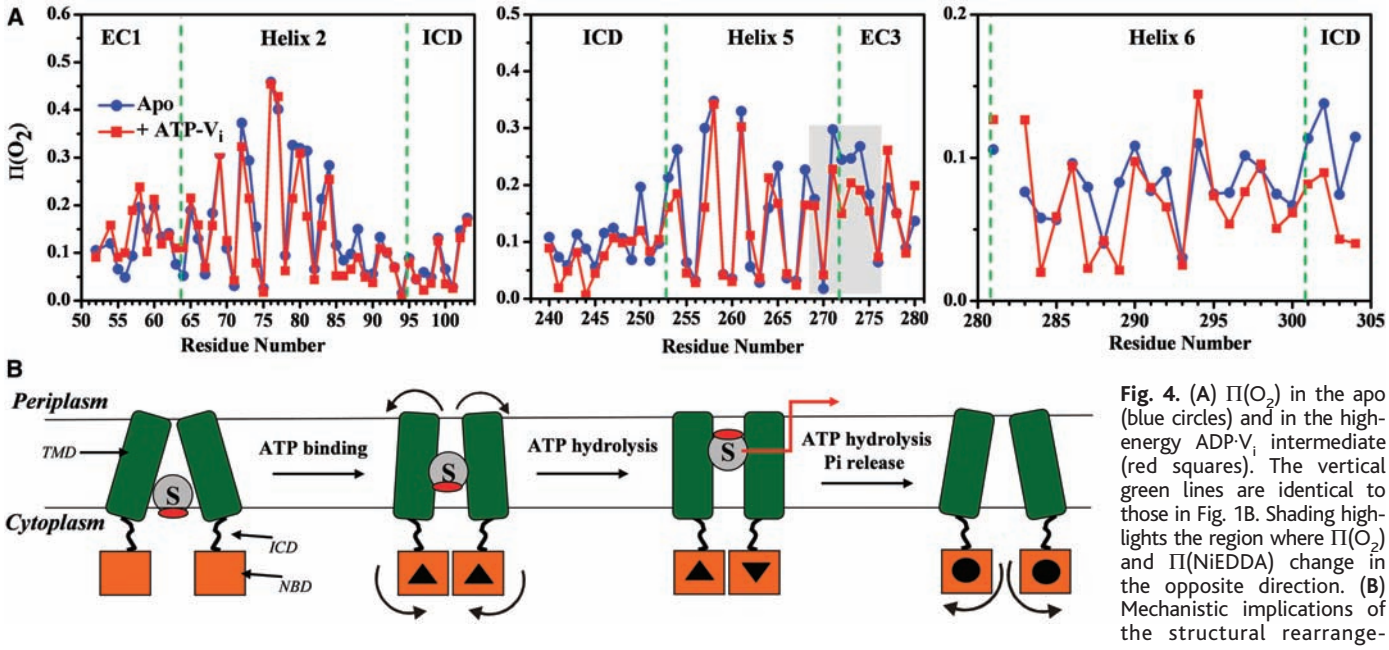

Fig. 4. (**A**) $\Pi(O_2)$ in the apo (blue circles) and in the high-energy ADP·V_i intermediate (red squares). The vertical green lines are identical to those in Fig. 1B. Shading highlights the region where $\Pi(O_2)$ and Π(NiEDDA) change in the opposite direction. (**B**) Mechanistic implications of the structural rearrangements. From an ensemble dominated by open-like conformers, ATP binding occludes the chamber, presumably through NBD dimerization, and increases water penetration at the periplasmic side. ATP hydrolysis accentuates the preference for closed-chamber conformations. At this stage, the amphipathic substrate senses equivalent dielectric environments at either side of the chamber and can partition to the bilayer or aqueous phases. The schematic shows the turnover of a single ATP molecule as implied by LmrA and P-gp biochemical studies. These studies also show that an intermediate with APD and P_i bound at a single NBD can rebind ATP and carry out another power stroke. In the low-energy ADP-bound state, chamber accessibility is restored, which allows the binding of another substrate molecule. ▲ Mg ·ATP; ▼ Mg ·ADP ·P_i; ● Mg ·ADP; S, substrate.

helix 6 (N terminus), and their interhelical loop (Fig. 3, A and B), areas of steady-state hydration in apo-MsbA. The changes in accessibility, accompanied by changes in mobilities along the 277 to 285 stretch, indicate extensive repacking (Fig. 2B).

Accessibilities and mobilities of the cytoplasmic region in the form populated by direct ADP and V_i addition are more similar to those obtained in the apo state (fig. S2). MsbA binds ADP as evidenced by the inhibition of ATP turnover (*22*). Therefore, the slow formation of the high-energy intermediate by addition of ADP and V_i demonstrates the presence of two post hydrolysis intermediates with different free energies.

The rigid-body movement that reduces the chamber accessibility does not change the phase of the oxygen accessibility patterns of helices 2 and 5, consistent with the absence of large-angle rigid helix rotation (Fig. 4A). Localized changes in $\Pi(O_2)$ amplitude associated with mobility changes (e.g., residues 72, 79, 83, 257, and 264 in Fig. 2B) indicate rearrangements in the backbone or tilting and translational motion relative to neighboring helices. In the 271 to 275 segment, ATP hydrolysis reduces O_2 accessibility (Fig. 4A, shaded region) and concomitantly increases NiEDDA accessibility (Fig. 3B), the types of changes anticipated as a result of increased hydration. Bending of helix 6 around a hinge provides a feasible model for the opposite change in distance at residue 292 versus residues 300 and 303 in the high-energy intermediate.

From the changes in the EPR constraints in trapped intermediates, we can reconstruct the protein rearrangements that mediate transition to a transport-competent state. The changes in Π(NiEDDA) mapped onto the open structure in Fig. 3D reveal simultaneous closing of the chamber and loosening of the periplasmic region initiated by ATP binding. Parallel changes in proximity establish the rigid-body nature of the underlying movement. The pattern of changes agrees with the model of alternate chamber exposure to each side or leaflet (*11*, *30*, *31*).

Correlation of the conformational cycle described here with previous biochemical data provides a plausible outline for the mechanism of transport (Fig. 4B). Substrate binding must precede chamber occlusion, i.e., it occurs before ATP binding, consistent with structural changes observed in two-dimensional crystals of P-gp (*32*). Crystal structures of isolated NBDs demonstrate that ATP binding drives NBD dimerization to form the ATP sandwich (*33*). The free energy of ATP is harnessed to close the chamber, which thereby traps the substrate, and the conformational changes are propagated to reconfigure the periplasmic side. ATP hydrolysis widens the periplasmic opening such that the ends of helices 5 and 6 at opposite sides of the transporter have similar levels of NiEDDA accessibility. The symmetrization of the chamber dielectric environment may act as a driving force for flipping and translocation of the amphipathic substrate (*12*, *13*). Hydrolysis of the second ATP molecule and inorganic phosphate (P_i) release move the NBDs apart, which restores chamber accessibility for another cycle.

Evidence of spectral heterogeneity in the EPR data set is consistent with shifts in the conformational equilibrium during the functional cycle. Starting from an ensemble of structures, ATP binding and hydrolysis shift the equilibrium toward states that have a closed chamber and a looser packing at the periplasmic side, although in none of the intermediates do the EPR constraints suggest a pure crystallographic closed state. The incremental nature of the structural changes on ATP hydrolysis suggests that ATP binding may provide the power stroke for transport. Although further analysis will be required to interpret the equilibrium data in terms of distinct conformers, the results provide a perspective on the flexibility of MDR ABC transporters and the conformational cycle that underlies their function.

References and Notes

1. C. F. Higgins, *Annu. Rev. Cell Biol.* **8**, 67 (1992).
2. C. F. Higgins, *Res. Microbiol.* **152**, 205 (2001).
3. H. Nikaido, J. A. Hall, *Methods Enzymol.* **292**, 3 (1998).
4. C. F. Higgins, R. Callaghan, K. J. Linton, M. F. Rosenberg, R. C. Ford, *Semin. Cancer Biol.* **8**, 135 (1997).
5. M. M. Gottesman, T. Fojo, S. E. Bates, *Nat. Rev. Cancer* **2**, 48 (2002).
6. H. W. van Veen, W. N. Konings, *Biochim. Biophys. Acta* **1365**, 31 (1998).
7. H. W. van Veen, W. N. Konings, *Adv. Exp. Med. Biol.* **456**, 145 (1998).
8. Z. Zhou, K. A. White, A. Polissi, C. Georgopoulos, C. R. Raetz, *J. Biol. Chem.* **273**, 12466 (1998).
9. W. T. Doerrler, C. R. Raetz, *J. Biol. Chem.* **277**, 36697 (2002).

10. G. Reuter *et al.*, *J. Biol. Chem.* **278**, 35193 (2003).
11. H. W. van Veen, C. F. Higgins, W. N. Konings, *Res. Microbiol.* **152**, 365 (2001).
12. G. Chang, C. B. Roth, *Science* **293**, 1793 (2001).
13. G. Chang, *J. Mol. Biol.* **330**, 419 (2003).
14. C. F. Higgins, K. J. Linton, *Science* **293**, 1782 (2001).
15. T. W. Loo, D. M. Clarke, *J. Biol. Chem.* **271**, 27482 (1996).
16. T. W. Loo, D. M. Clarke, *J. Biol. Chem.* **276**, 31800 (2001).
17. M. Seigneuret, A. Garnier-Suillerot, *J. Biol. Chem.* **278**, 30115 (2003).
18. D. R. Stenham *et al.*, *FASEB J.* **17**, 2287 (2003).
19. Starting with a cysteine-less MsbA background where the two native cysteines were replaced with alanines, we constructed 116 single-cysteine mutants. Only four mutations resulted in either weak or no expression (51, 53, 282) or slow aggregation after reaction with the spin label (78). MsbA mutants were spin labeled after Ni affinity chromatography, purified by size-exclusion chromatography (SEC) and then reconstituted in unilamellar vesicles. Details of the structural and functional analysis of the mutants are in the supporting material available on *Science* Online.
20. W. L. Hubbell, H. S. Mchaourab, C. Altenbach, M. A. Lietzow, *Structure* **4**, 779 (1996).
21. The collision frequency with paramagnetic reagents was deduced from the analysis of the saturation behavior of the spin label at each site. Power saturation curves were obtained under nitrogen gas, in the presence of 20% oxygen, or under nitrogen and in the presence of 50 mM NiEDDA. Distinct patterns of oxygen accessibility are expected for transmembrane segments, whereas exposure to the aqueous environments results in high NiEDDA accessibility. Spin-label mobility was estimated from the inverse of the central line width.
22. J. Dong, H. S. Mchaourab, unpublished observations.
23. G. J. Poelarends, W. N. Konings, *J. Biol. Chem.* **277**, 42891 (2002).
24. T. W. Loo, M. C. Bartlett, D. M. Clarke, *Biochemistry* **43**, 12081 (2004).
25. A. H. Buchaklian, A. L. Funk, C. S. Klug, *Biochemistry* **43**, 8600 (2004).
26. C. L. Reyes, G. Chang, *Science* **308**, 1028 (2005).
27. W. T. Doerrler, H. S. Gibbons, C. R. Raetz, *J. Biol. Chem.* **279**, 45102 (2004).
28. A. L. Davidson, *J. Bacteriol.* **184**, 1225 (2002).
29. I. L. Urbatsch, G. A. Tyndall, G. Tombline, A. E. Senior, *J. Biol. Chem.* **278**, 23171 (2003).
30. P. Mitchell, *Nature* **180**, 134 (1957).
31. P. Mitchell, *Res. Microbiol.* **141**, 286 (1990).
32. M. F. Rosenberg *et al.*, *EMBO J.* **20**, 5615 (2001).
33. P. C. Smith *et al.*, *Mol. Cell* **10**, 139 (2002).
34. E. F. Pettersen *et al.*, *J. Comput. Chem.* **25**, 1605 (2004).
35. We thank D. Piston, A. Beth, C. Cobb, H. Koteiche, and R. Nakamoto for critically reading the manuscript. This work was supported by a discovery grant from Vanderbilt University.

Supporting Online Material
www.sciencemag.org/cgi/content/full/308/5724/1023/DC1
Materials and Methods
Figs. S1 and S2
Table S1
References and Notes

21 October 2004; accepted 22 February 2005
10.1126/science.1106592

Structure of the ABC Transporter MsbA in Complex with ADP·Vanadate and Lipopolysaccharide

Christopher L. Reyes and Geoffrey Chang*

Select members of the adenosine triphosphate (ATP)–binding cassette (ABC) transporter family couple ATP binding and hydrolysis to substrate efflux and confer multidrug resistance. We have determined the x-ray structure of MsbA in complex with magnesium, adenosine diphosphate, and inorganic vanadate ($Mg{\cdot}ADP{\cdot}V_i$) and the rough-chemotype lipopolysaccharide, Ra LPS. The structure supports a model involving a rigid-body torque of the two transmembrane domains during ATP hydrolysis and suggests a mechanism by which the nucleotide-binding domain communicates with the transmembrane domain. We propose a lipid "flip-flop" mechanism in which the sugar groups are sequestered in the chamber while the hydrophobic tails are dragged through the lipid bilayer.

Multidrug resistance is an alarming and rapidly growing obstacle in the treatment of infectious diseases, human immunodeficiency virus (HIV), malaria, and cancer (*1*). Drug-resistant bacterial strains that cause gonorrhea, pneumonia, cholera, and tuberculosis are widespread and difficult to treat (*2*). In humans, a similar drug efflux mechanism is a major reason for the failure of several chemotherapeutics in the treatment of cancers. Found ubiquitously in both bacteria and humans, ABC transporters have been implicated in both antibiotic and cancer drug resistance and represent key targets for the development of agents to reverse multidrug resistance (*3*, *4*). Several MDR ABC efflux pumps have been shown to extrude both lipids and drug molecules, which suggests a common transport mechanism for amphipathic compounds across the cell membrane (*5*, *6*).

Department of Molecular Biology, The Scripps Research Institute, 10550 North Torrey Pines Road CB105, La Jolla, CA 92137, USA.

*To whom correspondence should be addressed. E-mail: gchang@scripps.edu

MsbA is an essential bacterial ABC transporter that transports lipid A and lipopolysaccharide (LPS) to the outer membrane (*7–10*) and that has been shown to have overlapping substrate specificity with the multidrug-resistant ABC (MDR ABC) transporter LmrA and with human P-glycoprotein (P-gp) (*11*). MsbA adenosine triphosphatase (ATPase) hydrolysis is stimulated by LPS and lipid A and also shows vanadate-inhibited activity (*12*). LPS makes up the outer leaflet of the outer membrane in Gram-negative bacteria and potently activates the mammalian innate immune system in response to bacterial infections; it can cause septic shock (*13–15*). ABC transporters are minimally composed of two transmembrane domains (TMDs) that encode substrate specificity and a pair of nucleotide-binding domains (NBDs) with conserved structural features. Comparison of the x-ray structures of MsbA and the vitamin B_{12} ABC importer, BtuCD, suggests that differences in substrate specificities are a consequence of structurally divergent TMDs (*16–18*). These structures, along with those derived from electron microscopy (EM) of other MDR ABC transporters, reveal that large conformational changes are possible in both the TMDs and NBDs (*19–23*).

Despite attempts to model the structural changes of MsbA and other MDR ABC transporters, a detailed view of conformational rearrangements during ATP hydrolysis and substrate translocation has remained elusive (*24*). What are the conformational changes of the TMDs during the catalytic cycle? What residues are involved in substrate binding and release? And what specific role does nucleotide binding and hydrolysis play during the catalytic cycle? To address these questions, we describe the structure of MsbA from *Salmonella typhimurium* in complex with adenosine 5′-diphosphate and inorganic vanadate ($ADP{\cdot}V_i$), Mg^{2+}, and rough-chemotype (Ra) lipopolysaccharide (Ra LPS). The structure provides evidence for an intermediate after ATP hydrolysis and a molecular basis for coupling ATP hydrolysis with amphipathic substrate transport.

Crystals of MsbA in complex with $Mg{\cdot}ADP{\cdot}V_i$ and Ra LPS were grown using detergent-solubilized protein incubated with Ra LPS purified from *S. typhimurium*. ATP, Mg^{2+}, and boiled sodium orthovanadate were added to favor the transition state conformation before crystallization (*25*). Mass spectrometry on washed crystals indicated the presence of Ra LPS, nucleotide, and vanadate. The structure was determined by single-wavelength anomalous dispersion (SAD), and the electron density maps were improved by using noncrystallographic symmetry averaging to a resolution of 4.2 Å (see table S1) (*26*). The asymmetric unit revealed two dimers of MsbA with clear electron density corresponding to a nucleotide and Ra LPS. The TMDs in each dimer exhibit a 30° torque relative to the molecular two-fold axis and an extensive interdigitation of the helices (Fig. 1, A and B). A chemical model with good geometry was built with R_{cryst} of 28% and R_{free} of 33%.

In this structure, each dimer contains two bound LPS molecules located at the protein-